Numerical simulation of a low-power hydrazine arcjet thruster

Hai-Xing Wang [a*], Jin-Yue Geng [a], Xi Chen [b], Wenxia Pan [c]

[a] School of Astronautics, Beijing University of Aeronautics and Astronautics, Beijing 100191, China
[b] Department of Engineering Mechanics, Tsinghua University, Beijing 100084, China
[c] Institute of Mechanics, Chinese Academy of Sciences, Beijing 100190, China

Abstract   A modeling study is conducted to investigate the plasma flow and heat transfer characteristics of low-power (kW class) arc-heated thrusters (arcjets) with 2:1 hydrogen/nitrogen to simulate decomposed hydrazine as the propellant. The all-speed SIMPLE algorithm is employed to solve the governing equations, which take into account the effects of compressibility, the Lorentz force and Joule heating, as well as the temperature- and pressure-dependence of the gas properties. Typical computed results about the temperature, velocity and Mach number distributions within arcjet thruster are presented for the case with arc current of 9 A and inlet stagnant pressure of 3.3×10^5 Pa to show the flow and heat transfer characteristics. It is found that the propellant is heated mainly in the near-cathode and constrictor region, with the highest plasma temperature appearing near the cathode tip, and the flow transition from the subsonic to supersonic regime occurs within the constrictor region. The effect of gas viscosity on the plasma flow within arcjet thruster is examined by an additional numerical test using artificially reduced values of gas viscosity. The test results show that the gas viscosity appreciably affects the plasma flow and the performance of the arcjet thruster for the cases with the hydrazine or hydrogen as the propellant. The integrated axial Lorentz force in the thruster nozzle is also calculated and compared with the thrust force of the arcjet thruster. It is found that the integrated axial Lorentz force is much smaller than the thrust force for the low-power arcjet thruster. Modeling results for the NASA 1-kW class arcjet thruster with simulated hydrazine as the propellant are found to be reasonably consistent with available experimental data.

Keywords: low-power arcjet, plasma flow and heat transfer, numerical modeling, hydrazine

---

* Corresponding author. Fax: +86 10 8233 9631; E-mail address: whx@buaa.edu.cn

Introduction

The arcjet thruster is a space propulsion system that uses a DC arc to heat propellant to a rather high temperature and thus can achieve a specific impulse appreciably higher than that of the conventional chemical thruster (*i.e.* rocket) or the resistance-heated thruster (*i.e.* resistojet). Low power arcjet thruster systems have been flight qualified and used successfully on the commercial geosynchronous satellites for their north-south station keeping (NSSK) [1-3]. With the increasing desire to reduce satellite launch costs and increase satellite service life, arcjet thrusters are destined to become one of standard electric propulsion thrusters for the satellite station-keeping and have been proposed for other propulsion applications such as for longitude correction and even for orbit transfer.

A typical arcjet thruster (see Fig. 1) consists of a cathode and a Laval-type anode-nozzle. The gaseous propellant is injected at the upstream and outflows from the nozzle with a supersonic velocity. The cathode sits in the upstream high-pressure side of the thruster nozzle. An electric arc is struck between the cathode tip and the anode-nozzle wall. The gasdynamic force of the gas flow pushes the arc passing through the constrictor so that the arc-root attachment occurs on the diverging segment of the anode-nozzle. The low gas pressure in this arc-root attachment region facilitates the formation of a diffuse mode of anode arc attachment. Complex physical phenomena are involved in the arcjet nozzle, including subsonic-supersonic flow, interaction between the electric arc and the plasma flow and heat transfer, coupled heat transfer between the gas flow region and the solid wall region, etc. Although many modeling and experimental results concerning arcjet thrusters have been conducted in recent decades [4-15] and a great amount of experimental and predicted results can be found in the literature concerning the arcjet thruster characteristics (*e.g.* specific impulses, thrust efficiency, arc voltages, etc.), our understanding on the complex flow and heat transfer processes within the arcjet thruster still remains incomplete.

Modeling studies are thus conducted in this paper to investigate the flow and heat transfer characteristics in the arcjet thruster. The radiation-cooled arcjet thruster designed by NASA Lewis Research Center, as shown in Fig. 1, which is extensively used in previous experimental and modeling studies of arcjet thrusters, is used in the present modeling study in order to compare the modeling predictions with the experimental data available in the literature.

Modeling approach

The main assumptions employed in the modeling study are as follows. (i) the gas flow in the arcjet nozzle is steady, axisymmetric, laminar and compressible; (ii) the bulk plasma is in the LTE (local thermodynamic equilibrium) state and thus the thermodynamic and transport properties of the plasma are completely determined by the gas temperature and pressure [16-18]; non-LTE effects are only considered by appropriately increasing the values of gas electrical conductivity in the near-anode region, as suggested in [8,9]; (iii) the plasma is optically thin to

radiation; (iv) the azimuthal (swirling) velocity component is negligible in comparison with the axial velocity component, and (v) the flow-induced electric field is negligible in comparison with the static electric field.

Based on these assumptions, the governing equations in the cylindrical coordinate system can be written as follows [5, 18].

Mass conservation equation

$$\frac{\partial}{\partial z}(\rho u) + \frac{1}{r}\frac{\partial}{\partial r}(r\rho v) = 0 \tag{1}$$

Momentum conservation equations

$$\frac{\partial(\rho uu)}{\partial z} + \frac{1}{r}\frac{\partial(r\rho uv)}{\partial r} = -\frac{\partial p}{\partial z} + 2\frac{\partial}{\partial z}\left(\mu\frac{\partial u}{\partial z}\right) + \frac{1}{r}\frac{\partial}{\partial r}\left[r\mu\left(\frac{\partial u}{\partial r} + \frac{\partial v}{\partial z}\right)\right] + j_r B_\theta \tag{2}$$

$$\frac{\partial(\rho uv)}{\partial z} + \frac{1}{r}\frac{\partial(r\rho vv)}{\partial r} = -\frac{\partial p}{\partial r} + \frac{2}{r}\frac{\partial}{\partial r}\left(r\mu\frac{\partial v}{\partial r}\right) + \frac{\partial}{\partial z}\left[\mu\left(\frac{\partial v}{\partial z} + \frac{\partial u}{\partial r}\right)\right] - 2\mu\frac{v}{r^2} - j_z B_\theta \tag{3}$$

Energy conservation equation

$$\frac{\partial(\rho uh)}{\partial z} + \frac{1}{r}\frac{\partial(\rho rvh)}{\partial r} = \frac{\partial}{\partial z}\left(\frac{\kappa}{c_P}\frac{\partial h}{\partial z}\right) + \frac{1}{r}\frac{\partial}{\partial r}\left(r\frac{\kappa}{c_P}\frac{\partial h}{\partial r}\right) + u\frac{\partial p}{\partial z} + v\frac{\partial p}{\partial r}$$

$$+ \Phi + \frac{j_z^2 + j_r^2}{\sigma} + \frac{5k_B}{2e}\left(\frac{j_z}{c_P}\frac{\partial h}{\partial z} + \frac{j_r}{c_P}\frac{\partial h}{\partial r}\right) - U_r \tag{4}$$

Electric potential (current continuity) equation

$$\frac{1}{r}\frac{\partial}{\partial r}\left(r\sigma\frac{\partial \phi}{\partial r}\right) + \frac{\partial}{\partial z}\left(\sigma\frac{\partial \phi}{\partial z}\right) = 0 \tag{5}$$

Here u and v are the axial (z-) and radial (r-) components of the velocity vector V, p and ϕ the gas pressure and electric potential, and k_B and e are the Boltzmann constant and elementary charge, respectively. The physical properties ρ, c_p, h, μ, κ, σ and U_r are the temperature- and pressure-dependent gas mass density, specific heat at constant pressure, specific enthalpy, viscosity, thermal conductivity, electrical conductivity and radiation power per unit volume of plasma, respectively, and are calculated for each spatial point based on local temperature and pressure by using pre-compiled LTE plasma property databases (covering the temperature range 300 K – 30000 K and pressure range 10 Pa – 3×10^5 Pa). The symbol Φ in Eq. (4) denotes the viscous dissipation term, and is calculated by

$$\Phi = \mu\left\{2\left[\left(\frac{\partial v}{\partial r}\right)^2 + \left(\frac{v}{r}\right)^2 + \left(\frac{\partial u}{\partial z}\right)^2\right] + \left(\frac{\partial v}{\partial z} + \frac{\partial u}{\partial r}\right)^2 - \frac{2}{3}(\nabla\cdot V)^2\right\} \tag{6}$$

The pressure work and viscous dissipation terms have been included in the energy equation (4) since they would be non-negligible for the compressible flow in the arcjet nozzle. The Lorentz force terms have been included in the momentum equations (2) and (3) and the Joule heating rate and the electron-enthalpy transport terms have been included in the energy equation

(4) in order to include the effects on the plasma flow and heat transfer of electromagnetic fields related to the DC electric arc discharge. Current density components j_r and j_z appearing in Eqs. (2), (3) and (4) are calculated by using

$$j_r = -\sigma \frac{\partial \phi}{\partial r} \qquad j_z = -\sigma \frac{\partial \phi}{\partial z} \qquad (7)$$

while the self-induced magnetic induction intensity B_θ is calculated by using

$$B_\theta = \frac{\mu_0}{r} \int_0^r j_z \xi d\xi \qquad (8)$$

where μ_0 is the permeability of free space.

The LTE assumption has been employed here as in most DC arc modeling studies. It is expected that non-LTE effects would exist (*e.g.* the electron temperature is always higher than the heavy-particle temperature in the arc-root region) and may affect the plasma flow, heat transfer and energy conversion within the arcjet thruster. The main problem of employing the LTE assumption is that it leads to significantly underestimated values of the gas electrical conductivity in the near-electrode region, in which the electron temperature is expected to be significantly higher than the heavy-particle temperature [18], and thus affects the arc current flow. Refs. [8,9] showed that using the LTE assumption for the bulk plasma flow but appropriately increasing the values of the electrical conductivity in the near-anode region to compensate the non-LTE effects can give reasonable modeling results of arcjet thruster characteristics. Ref. [8] used the following formula to calculate the gas electrical conductivity σ_n in the near-anode region when the local gas temperature is less than 10 000 K:

$$\sigma_n = (\sigma_{10000} - \sigma_{min}) T / 10000 + \sigma_{min} \quad \text{S/m} \qquad (9)$$

where σ_{min} is a defined value that can be empirically adjusted to obtain reasonable arc voltage ($\sigma_{min} = 10$ S/m is used in [8]), and σ_{10000} is the gas electrical conductivity at 10 000 K for the LTE plasma. For the region with temperatures T higher than 10 000 K, the LTE value of σ is used. This approach is also employed in this study to treat the arc-root attachment at the inner surface of the anode-nozzle.

Differently from many previous studies, the temperature distribution along the inner surface of the anode-nozzle is determined by the iterative computation process itself in this study, instead of being artificially specified [8,9]. To this end we employ a computational domain (see Fig. 1) that includes both the gas flow region inside the thruster nozzle and the solid wall region (anode-nozzle wall), and the energy equation (4) is solved for both the gas region and the solid region in a unified way [5].

Due to the axisymmetry of the thruster nozzle, only the upper half of the thruster nozzle is taken into account in the computation. The computational domain used in the modeling is denoted as A-B-C-D-E-F-G-H-A in Fig. 1, in which A-B-H-A is the cathode, C-D-E-F-J-I-C is

the anode-nozzle wall, whereas C-I, I-J and J-F are the inner surfaces of the convergent segment, cylindrical segment (constrictor) and divergent segment of the anode-nozzle.

The boundary conditions used in the computation are as follows. At the gas-inlet section of the arcjet nozzle (*i.e.* at B-C in Fig. 1), the gas stagnant pressure is set to 3.3×10^5 Pa, the gas temperature is taken to be 500 K, the radial velocity component $v = 0$ and the axial velocity component u is calculated from the given inlet stagnant pressure p_0 and the computed local static pressure p (obtained by extrapolating the static pressures at the interior grid points neighboring the inlet boundary) using the following compressible flow relation:

$$\left(\frac{p_0}{p}\right)^{(\gamma-1)/\gamma} = 1 + \left(\frac{\gamma-1}{2}\right)\frac{u^2}{\gamma RT} \tag{10}$$

in which γ is the ratio of specific heats and R is the ideal gas constant. The mass flow rate of incoming propellant is determined by the computational process itself, as in Ref. [19].

The temperatures at the upstream boundary of the anode-nozzle (C-D) are obtained by extrapolating the temperatures at the interior grid points neighboring the upstream boundary of the anode-nozzle wall. On the outer surfaces D-E and E-F, the local heat flux is governed by the thermal radiation to cold surroundings (300 K) and an emissivity of $\varepsilon = 0.3$ is used for the tungsten nozzle.

Zero velocity components are specified at all solid boundaries; axisymmetric conditions are employed along the nozzle axis; and the temperatures and velocities at the exit section of the thruster are calculated in the iteration process by extrapolating their values at the interior grid points neighboring the outlet boundary.

Zero current densities are assumed at all the boundaries except for the cathode or anode. The cathode body is included in the calculation domain, and at the rear end of cathode (A-B in Fig. 1) $u = 0$, $v = 0$, $T = 1000$ K and $\partial\phi/\partial z = I/(A\sigma_c)$ are used, where I, A and σ_c are the arc current, cathode end area, and the electrical conductivity of cathode material. $\phi = 0$ is set at the outer surfaces of thruster D-E.

The governing equations are solved using a computer program [19], which is a version of the FAST-2D program [20] modified to include variable gas properties and compressible effects. The all-speed SIMPLE algorithm [19], which is incorporated into the modified FAST-2D program to simulate the subsonic–supersonic flow, is used to solve the governing equations (1) – (5), associated with the auxiliary relations (6) – (10) and the specified boundary conditions, to obtain the distributions of the velocity components, pressure and specific enthalpy (or temperature) within the whole thruster nozzle. Altogether 89 (z-direction)$\times$ 30 (r-direction) grid points are employed in this study. Mass conservation is ensured in the computation, *i.e.* the axial mass flux of the propellant is constant for all cross-sections of the nozzle.

Results and Discussion

For a fixed gas stagnant-pressure (3.3×10^5 Pa) at the nozzle inlet and a constant arc current of 9 A, typical modeling results are presented in Figs. 2 – 3 concerning the plasma flow and heat transfer characteristics of the arcjet thruster (see Fig. 1) using simulated hydrazine as the propellant.

Figure 2 (a) plots the computed temperature distributions in the gas flow region and in the solid-wall region of the nozzle. Fig. 2 (a) shows that the gaseous propellant entering into the thruster undergoes a rapid temperature rise in the near-cathode and constrictor region due to arc heating (Joule heating). Subsequently the heated high-temperature partially-ionized gas (plasma) expands in the diverging part of the nozzle, accompanying by an appreciable temperature decrease in the axial direction in the nozzle. As expected, there exist large radial gradients of the gas temperature in the thruster nozzle, especially in the constrictor region and near the gas-solid interface.

The computed axial velocity and Mach number distributions within the thruster nozzle are presented in Fig. 2 (b) and Fig. 2 (c), respectively. Fig. 2 (b) shows that due to the conversion of the pressure energy and internal energy into the kinetic energy, the gaseous propellant flowing into the nozzle is rapidly accelerated to rather high velocities within a short axial distance. There also exist large radial gradients of the axial velocity in the thruster nozzle. Unlike the conventional compressible flow in a Laval nozzle, the maximum velocity is found to appear in the interior of the arcjet nozzle (at the location near the downstream end of the constrictor) instead of at the nozzle exit. Fig. 2 (c) shows that the Mach number (*i.e.* the ratio of local flow velocity to local sound speed) monotonically increases in the axial direction, the flow transits from the subsonic to the supersonic regime (*i.e.* from Ma < 1 to Ma > 1) within the constrictor region, and the flow becomes completely supersonic (Ma > 1) in the diverging segment of the thruster nozzle.

Figure 3 (a) shows the computed variations along the nozzle axis of the plasma temperature and axial velocity, respectively, for the simulated-hydrazine arcjet thruster. Fig. 3 (a) clearly shows that the along the axis, plasma temperature increases very rapidly at first due to the arc heating in the near-cathode and constrictor region, assumes its maximum value near the downstream end of the constrictor region, and then decreases quite rapidly to comparatively low values as the hot gas expands in the divergent segment of the nozzle. The highest plasma temperatures appearing in the rapid-heating region are 18 480 K for the case with the arc current of 9 A. The axial velocity distribution along the thruster axis also shown in Fig. 3 (a) is somewhat different from the on-axis temperature distribution. The axial velocity increases rapidly at first until a maximum is achieved, and then decreases gradually as the propellant flows towards the thruster exit. The axial velocity assumes its maximum value at the axial location about 0.55 mm downstream of the constrictor as a result of the complex interaction between the Joule heating, Lorentz force, viscous force and thermodynamic expansion. In the divergent segment of the thruster nozzle, the axial velocity at the nozzle axis decreases from the maximum value of 8716

m/s to an appreciably lower value 6635 m/s at the thruster exit. Figure 3 (b) shows the computed radial distributions of the gas temperature and axial velocity at the nozzle exit plane (F-G in Fig. 1). It shows that the predicted highest temperature at the centre of thruster exit plane is 2223 K for the case with the arc current of 9 A.

As mentioned above and seen in Fig. 3 (a), the fact that the highest axial velocity always appears inside the nozzle instead of at the nozzle exit is a point of difference between the arcjet nozzle flow and the conventional compressible flow in a Laval nozzle. It is often considered that viscous transport is responsible for this flow behavior, and some experimental results concerning the radial profiles of axial velocities at three different axial positions within arcjet nozzle are presented in Ref. [15] to support this judgment. It was found that while the centerline velocity decreased along the nozzle axis the radial profile was flattened, indicating the existence of appreciable radial transport of the axial momentum away from the nozzle centerline.

Since the full Navier-Stokes equations are employed in our modeling, we can artificially change the gas viscosity to examine how the values of gas viscosity affect the modeling results in some details. In the computation, the gas viscosity at each grid point is artificially set to be $\mu_{art} = 0.1\mu$, *i.e.*, using significantly reduced values of gas viscosity, and the obtained modeling results with $\mu_{art} = 0.1\mu$ are compared with those for the original case with actual viscosity. Besides the case for the simulated-hydrazine arcjet with the arc current of 9 A and the inlet stagnation pressure of 3.3×10^5 Pa, the modeling results with $\mu_{art} = 0.1\mu$ and with actual viscosity are also compared for the hydrogen arcjet thruster with the arc current of 10 A and the inlet stagnation pressure of 2.5×10^5 Pa.

Figure 4 compares the computed variations of the axial velocity and temperature along the nozzle axis for the case using $\mu_{art} = 0.1\mu$ to the original results using actual viscosity values. Corresponding comparison is shown in Fig. 5 concerning the computed radial distributions of the axial velocity and gas temperature at the nozzle exit plane. It is seen from Fig. 4 (a) and Fig. 5 (a) that for the simulated-hydrazine arcjet thruster, the axial velocity along the nozzle axis decreases from the maximum value 12 303 m/s to 10570 m/s for the case using $\mu_{art} = 0.1\mu(T, p)$, while the axial velocity along the nozzle axis decreases from the maximum values of 8716 m/s to 6635 m/s for the case using actual gas viscosity values. Correspondingly, for the hydrogen arcjet thruster, the axial velocity along the nozzle axis decreases from the maximum values of 32 018 m/s to 20 380 m/s for the case using $\mu_{art} = 0.1\mu(T)$, while the axial velocity along the nozzle axis decreases from the maximum values of 22 429 m/s to 12 210 m/s for the case using actual gas viscosity values. These results demonstrate that the values of gas viscosity have significant effects on the plasma flow within the arcjet thruster. The effects of the gas viscosity on the plasma flow in the hydrogen (with smaller molecular weight) arcjet thruster are somewhat more appreciable than those in the simulated-hydrazine arcjet thruster. Fig. 4 (b) and Fig. 5 (b) show

that the gas viscosity only slightly affects the temperature distributions within the arcjet thruster. The corresponding comparison of performance parameters of arcjet thruster for the cases with the actual viscosity and the artificially reduced viscosity are shown in Table 1 and 2. It is seen in Table 1 that for the case with the arc current of 9 A and the inlet stagnation pressure of 3.3×10^5 Pa, when the artificial gas viscosity μ_{art} is set to be 0.1μ, the arc voltage, mass flow rate, thrust and specific impulse of simulated-hydrazine arcjet thruster would increase by 1.7 %, 2.7 %, 23.1 % and 19.8 %, respectively, over that of the case using the actual viscosity. Correspondingly, as seen in Table 2, for the case with the arc current of 10 A and the inlet stagnation pressure of 2.5×10^5 Pa, when the artificial gas viscosity μ_{art} is set to be 0.1μ, the arc voltage, mass flow rate, thrust and specific impulse of hydrogen arcjet thruster would increase by 0.9 %, 6.0 %, 39.0 % and 31.8 %, respectively, over that of the case using the actual viscosity. It is clear from Table 1 and 2, that the gas viscosity significantly affects the performance of the arcjet thruster.

In the arcjet thruster, the interaction between the arc current and the induced magnetic field would generate a Lorentz force. It is interesting to compare the integrated axial Lorentz force with the thrust force produced by the arcjet thruster. In our modeling, the integrated axial Lorentz force $F_{Lorentz}$ is calculated by

$$F_{Lorentz} = \int_0^L \int_0^{R_z} j_r B_\theta 2\pi r dr dz \tag{11}$$

Here R_z is the radius of the nozzle cross-section at the axial location z, while the L is the total length of the arcjet nozzle. Typical calculated results are shown in Table 3 for the arcjet thrusters using simulated hydrazine and hydrogen, respectively, as the propellants. It is seen that the integrated axial Lorentz force is about 0.016% of the total thrust force for the simulated-hydrazine arcjet thruster, whereas this percentage is about 0.053% for the hydrogen arcjet thruster. Namely, the integrated axial Lorentz force is always negligible small in comparison with the thrust force of the arcjet thruster.

Many experimental results have been reported in the literature about the kW-class arcjet thruster designed by the NASA Lewis Research Center (shown in Fig. 1) and using simulated hydrazine as the propellant [6,7,15,21,23-25]. Hence, we can compare our modeling results with the experimental data available in the literature for the similar operating parameters.

Figure 6 compares the predicted gas temperature variation along the nozzle axis with the experimental data reported in Ref. [23]. In the experiment, simulated hydrazine was used as the propellant, the mass flow rate was 47.6 mg/s, the arc current was 9 A, and the N_2 vibrational and rotational temperatures were determined by measuring the emission spectra of the plasma at the nozzle axis through a few holes drilled through the nozzle wall. The modeling results shown in Fig. 6 (a) were obtained for the case with the arc current of 9 A and the mass flow rate of 44.8 mg/s. Although there is a little difference between the mass flow rate obtained in the modeling and that used in the experiment, Fig. 6 shows that the predicted centerline temperature variation agrees reasonably well with the experimental data.

Refs. [24, 25] used a spatially resolved time-of-flight (TOF) electrostatic probe to measure the radial profile of the plasma axial-velocity at the arcjet thruster exit plane for the case with the 1:2 nitrogen/hydrogen mixture to simulate hydrazine as the propellant. The arc current was 10 A and the mass flow rate was 50 mg/s. The measured arc voltage and the specific impulse were 112 V and 420 s, respectively. Correspondingly, the modeling results have been obtained for the simulated-hydrazine arcjet with the arc current of 10 A and the mass flow rate of 50.1 mg/s. The predicted arc voltage and specific impulse were 90.7 V (the sheath voltage is not included) and 412 s. Fig. 6 (b) shows that our predicted radial profile of the axial velocity at the nozzle exit also agrees well with the measured results of the TOF probe [24,25], although the predicted radial profile of the axial velocity is somewhat narrower than the measured one. The narrower radial profile is predicted partially because the modeling results are shown for the nozzle exit, while the TOF probe measurement was conducted in the near-exit plume. In addition, rarefied gas effect is not considered in the modeling.

Although LTE is assumed, with the only non-LTE effect included being an increased gas electrical conductivity in the near-anode region, the modeling predictions are reasonably consistent with available experimental results for the simulated hydrazine arcjet thrusters. It is expected that the present modeling approach is also useful for other cases involving arc-heated supersonic flow. However, the predicted results for the arc voltage and arc-root attachment are not yet satisfactory. Further improvement of the model is required in subsequent studies.

Conclusions

Numerical simulations have been carried out to study the plasma flow and heat transfer characteristics of low-power (kW class) arcjet thrusters with the simulated hydrazine as the propellant. The modeling results show that the propellant is heated mainly by Joule heating in the near-cathode and constrictor region with the highest plasma temperature appearing near the cathode tip, and the highest axial velocity appears inside the diverging nozzle (near the downstream end of the constrictor) instead of at the nozzle exit. In order to examine the effect of gas viscosity on the flow and heat transfer characteristics of the arcjet thruster, artificially reduced values of gas viscosity, *i.e.* $\mu_{art} = 0.1\mu(T, p)$ is used to substitute the actual gas viscosity in a special numerical test, and the test results show that gas viscosity values have significant effect on the plasma flow and heat transfer as well as on the performance of the arcjet thruster. Since the molecular weight of hydrogen is much smaller, the viscous effect is more appreciable for the hydrogen arcjet thruster than that for the simulated-hydrazine arcjet thruster. The integrated axial Lorentz force is also calculated in our modeling and compared with the thrust force of the arcjet thruster, and the former is shown to be always much less than the latter for the arcjet thruster. Modeling results for the NASA 1-kW class arcjet thruster with simulated hydrazine as the propellant are found to compare favorably with the experimental data available in the literature.

References

[1] R.H. Frisbee (2003) Advanced Space Propulsion for the 21st Century. Journal of Propulsion and Power **19**: 1029-1154

[2] G.W. Butler, R.J. Cassady (1996) Directions for Arcjet Technology Development. Journal of Propulsion and Power **12**: 1026-1034

[3] M.A. Birkan (1996) Arcjets and Arc Heaters: An Overview of Research Status and Needs. Journal of Propulsion and Power **12**: 1011-1017

[4] V.R. Watson, E.B. Pegot (1967) Numerical Calculations for the Characteristics of a Gas Flowing Axially Through a Constricted Arc. NASA Technical Note TN D-4042

[5] H.X. Wang, X. Chen, W.X. Pan, A.B. Murphy, J.Y. Geng, S.X. Jia (2010) Modelling Study to Compare the Flow and Heat Transfer Characteristics of Low-Power Hydrogen, Nitrogen and Argon Arc-Heated Thrusters. Plasma Science and Technology **12** (in press)

[6] M.A. Cappelli, P.V. Storm (1996) Interior Plasma Diagnostics of Arcjets Thrusters. Journal of Propulsion and Power **12**: 1070-1076

[7] P.V. Storm, M.A. Cappelli (1996) LIF Characterization of Arcjet Nozzle Flows. AIAA Paper No 96-2987

[8] R.P. Rhodes, D. Keefer (1990) Numerical Modeling of an Arcjet Thruster. AIAA Paper No. 90-2614

[9] G.W. Bulter, D.Q. King (1992) Single and Two Fluid Simulations of Arcjet Performance. AIAA Paper No 92-3104

[10] G.W. Bulter, A.E. Kull, D.Q. King (1994) Single Fluid Simulations of Low Power Hydrogen Arcjet. AIAA Paper No 94-2870

[11] D. Burtner, D. Keefer, W. Ruyten (1994) Experimental and Numerical Studied of a Low-Power Arcjet Operated on Simulated Ammonia. AIAA Paper No 94-2869

[12] D. Burtner, D. Keefer, W. Ruyten (1996) Low-Power Ammonia Arcjet: Numerical Simulations and Laser-Induced Fluorescence Measurements. Journal of Propulsion and Power **12**: 1123-1128

[13] J.G. Liebeskind, R.K. Hanson, M.A. Cappelli (1994) Flow Diagnostics of an Arcjet Using Laser-Induced Fluorescence. AIAA Paper No. 92-3243

[14] D. Keefer, D. Burtner, T. Moeller, R. Rhodes (1994) Multiplexed Laser Induced Fluorescence and Non-Equilibrium Processes in Arcjets. AIAA Paper No. 94-2656

[15] P.V. Storm, M.A. Cappelli (1998) Arcjet Nozzle Flow-Field Characterization by Laser-Induced Fluorescence. Applied Optics **37**: 486-495

[16] A.B. Murphy, C.J. Arundell (1994) Transport Coefficients of Argon, Nitrogen, Oxygen, Argon-Nitrogen, and Argon-Oxygen Plasmas. Plasma Chemistry and Plasma Processing **14**: 451-490

[17] A.B. Murphy (2000) Transport Coefficients of Hydrogen and Argon-Hydrogen Plasmas. Plasma Chemistry and Plasma Processing **20**: 279-297

[18] X. Chen (2009) Heat Transfer and Fluid Flow under Thermal Plasma Conditions. Science Press, Beijing. Chapter 3 (in Chinese)

[19] P. Han, X. Chen (2001) Modeling of the Subsonic–Supersonic Flow and Heat Transfer in a DC Arc Plasma Torch. Plasma Chemistry and Plasma Processing **21**: 249-264

[20] J. Zhu (1991) FAST-2D: A Computer Program for Numerical Simulation of Two-Dimensional Incompressible Flows with Complex Boundaries. Institute for Hydromechanics. University of

Karlsruhe, Report No. 690

[21] R.L. Burton, S.A. Bufton (1996) Exit-Plane Electrostatic Probe Measurements a Low-Power Arcjet. Journal of Propulsion and Power **12**: 1099-1106

[22] S.A. Miller (1994) Multifluid Nonequilibrium Simulation of Arcjet thrusters, PhD, thesis, Massachusetts Institute of Technology

[23] D.M. Zube, R.M. Myers (1993) Thermal Nonequilibrium in a Low-Power Arcjet Nozzle. Journal of Propulsion and Power **9**: 545-552

[24] S.A. Bufton, R.L. Burton (1997) Velocity and Temperature Measurements in a Low-Power Hydrazine Arcjet. Journal of Propulsion and Power **13**: 768-774

[25] S.A. Bufton, R.L. Burton (1995) Measured Plasma Properties at the Exit Plane of a 1 kW Arcjet. AIAA Paper No 95-3066

Figure Captions

Fig. 1 Schematic diagrams of the kW-class arcjet thrusters under study. The geometrical sizes and the computational domain (A-B-C-D-E-F-G-H-A) are also shown.

Fig. 2 Computed isotherms within the gas flow region and the solid wall region (a), axial velocity contours within the nozzle (b) and Mach number contours within the nozzle (c) for the arcjet thruster with simulated hydrazine as the propellant. Inlet stagnant pressure is $3.3{\times}10^5$ Pa and arc current is 9 A.

Fig. 3 Computed axial velocity and temperature variations along the nozzle axis (a) and computed axial velocity and temperature profiles at the nozzle exit plane (b) for the arcjet thruster with simulated hydrazine as the propellant. Inlet stagnant pressure is $3.3{\times}10^5$ Pa and arc current is 9 A.

Fig. 4 Comparisons of computed axial velocity (a) and temperature (b) variations along the nozzle axis for different viscosity values. CASE 1: with simulated hydrazine as the propellant, inlet stagnant pressure $3.3{\times}10^5$ Pa and arc current 9 A; and CASE 2: with pure hydrogen as propellant, inlet stagnant pressure $2.5{\times}10^5$ Pa and arc current 10 A. 1.0μ means actual viscosity is used; 0.1μ means 0.1 times actual viscosity is used.

Fig. 5 Comparisons of computed axial velocity (a) and temperature (b) profiles at the exit plane for different viscosity values. CASE 1: with simulated hydrazine as the propellant, inlet stagnant pressure $3.3{\times}10^5$ Pa and arc current 9 A; and CASE 2: with pure hydrogen as propellant, inlet stagnant pressure $2.5{\times}10^5$ Pa and arc current 10 A. 1.0μ means actual viscosity is used; 0.1μ means 0.1 times actual viscosity is used.

Fig. 6 Comparisons of computed results and experimental data concerning the axial variation of gas temperature along the nozzle axis (a) and the radial profile of axial-velocity at the exit plane (b) for the simulated hydrazine arcjet. The arc current is 9 A for (a) and 10 A for (b).

Table 1 Comparisons of predicted performance parameters of the arcjet thruster with simulated hydrazine as propellant for the cases using artificial viscosity μ_{art} (=0.1μ) and actual viscosity (μ), respectively, in the computation. Inlet stagnant pressure is 3.3×10^5 Pa and arc current is 9 A.

Table 2 Comparisons of predicted performance parameters of the arcjet thruster with hydrogen as propellant for the cases using artificial viscosity μ_{art} (=0.1μ) and actual viscosity (μ), respectively, in the computation. Inlet stagnant pressure is 2.5×10^5 Pa and arc current is 10 A.

Table 3 Calculated values of the integrated axial Lorentz forces and the thrust force of the arcjet thruster. CASE 1: for the case with simulated hydrazine as the propellant, and the inlet stagnant pressure and arc current are 3.3×10^5 Pa and 9 A, respectively. CASE 2: for the case with hydrogen as the propellant, and the inlet stagnant pressure and arc current are 2.5×10^5 Pa and 10 A, respectively.

	Current (A)	Voltage (V)	Mass flow rate (mg/s)	Thrust (mN)	I_{sp} (s)
μ	9	100.3	44.8	186	424
0.1μ	9	102.0	46.0	229	508
△%		1.7%	2.7%	23.1%	19.8%

	Current (A)	Voltage (V)	Mass flow rate (mg/s)	Thrust (mN)	I_{sp} (s)
μ	10	101.7	15.0	118	800
0.1μ	10	102.6	15.9	164	1054
△%		0.9%	6.0%	39.0%	31.8%

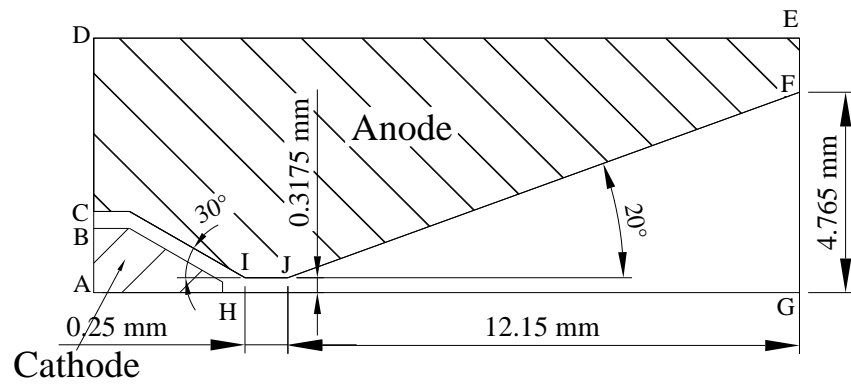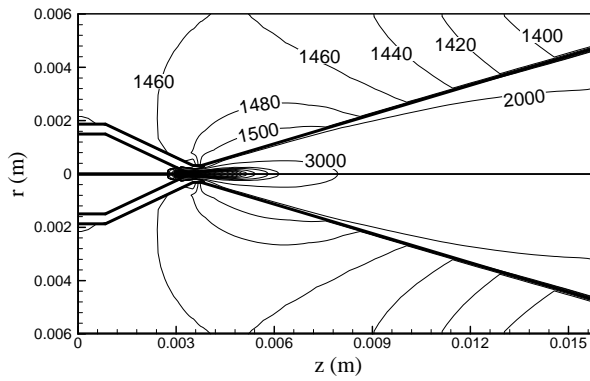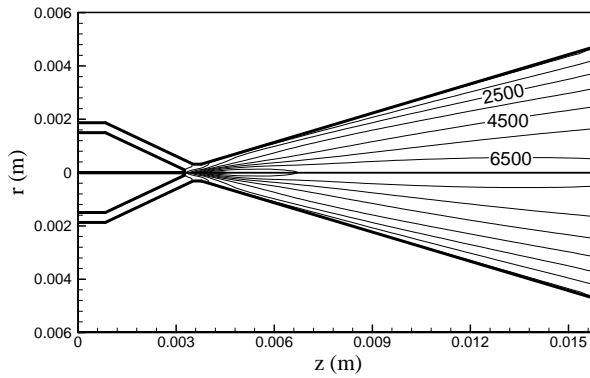|	Lorentz force (mN)	Thrust (mN)	Lorentz force/Thrust
CASE 1	2.98×10^{-2}	186	0.016%
CASE 2	6.16×10^{-2}	117	0.053%

Fig. 1 Schematic diagrams of the kW-class arcjet thrusters under study. The geometrical sizes and the computational domain (A-B-C-D-E-F-G-H-A) are also shown.

(a) Computed isotherms within the gas region and the solid region.
Isotherm interval in the gas-phase region is 1000 K.

(b) Computed axial velocity contours within the nozzle. Isoline interval: 1000 m/s.
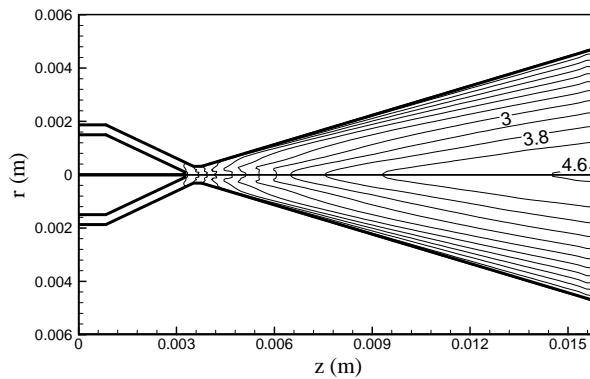
(c) Computed Mach number contours within the nozzle. Isoline interval: 0.4.

Fig. 2 Computed isotherms within the gas flow region and the solid wall region (a), axial velocity contours within the nozzle (b) and Mach number contours within the nozzle (c) for the arcjet thruster with simulated hydrazine as the propellant. Inlet stagnant pressure is 3.3×10^5 Pa and arc current is 9 A.
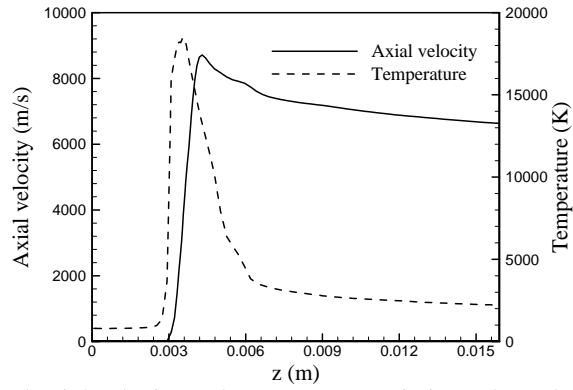
(a) Computed axial velocity and temperature variations along the nozzle axis.
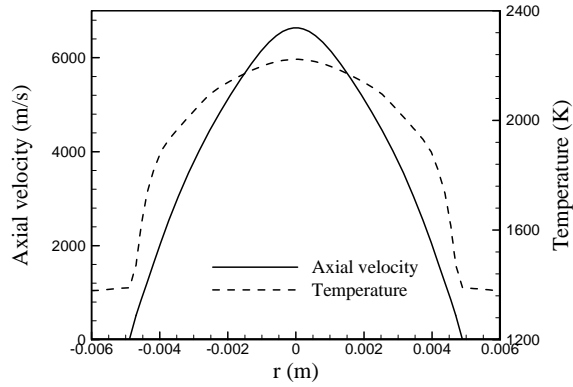
(b) Computed axial velocity and temperature profiles at the nozzle exit plane.

Fig. 3 Computed axial velocity and temperature variations along the nozzle axis (a) and computed axial velocity and temperature profiles at the nozzle exit plane (b) for the arcjet thruster with simulated hydrazine as the propellant. Inlet stagnant pressure is 3.3×10^5 Pa and arc current is 9 A.

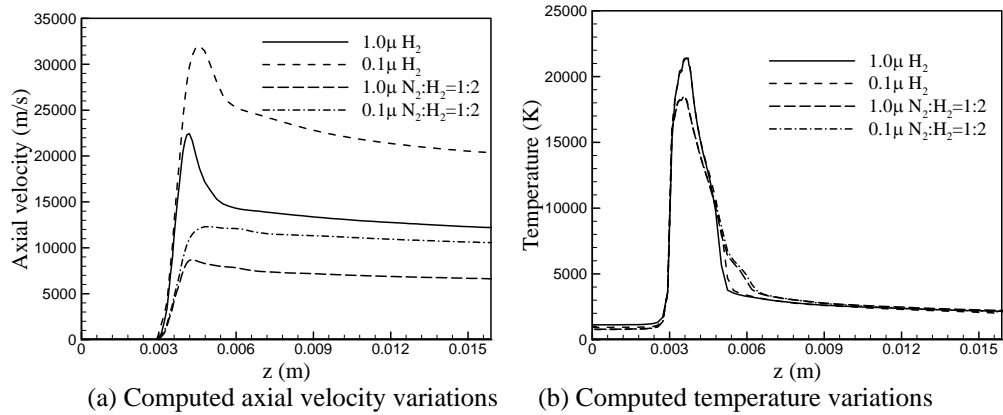(a) Computed axial velocity variations   (b) Computed temperature variations

Fig. 4 Comparisons of computed axial velocity (a) and temperature (b) variations along the nozzle axis for different viscosity values. CASE 1: with simulated hydrazine as the propellant, inlet stagnant pressure 3.3×10^5 Pa and arc current 9 A; and CASE 2: with pure hydrogen as propellant, inlet stagnant pressure 2.5×10^5 Pa and arc current 10 A. 1.0μ means actual viscosity is used; 0.1μ means 0.1 times actual viscosity is used.

(a) Computed axial velocity profiles   (b) Computed temperature profiles
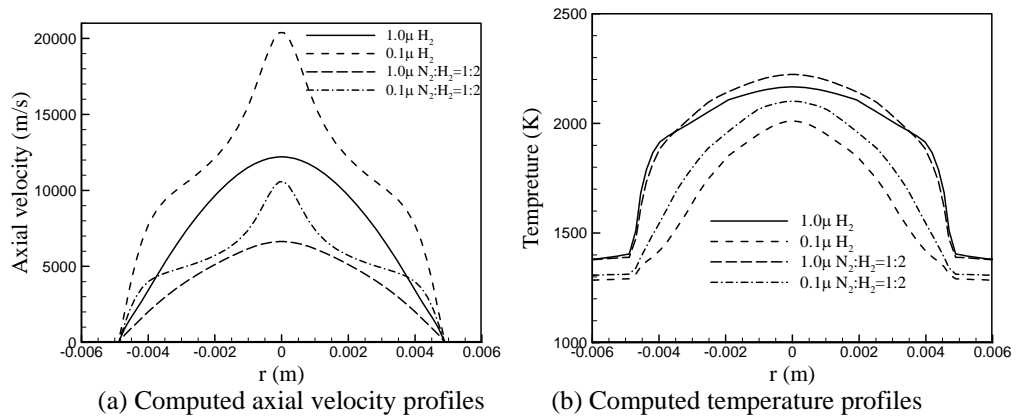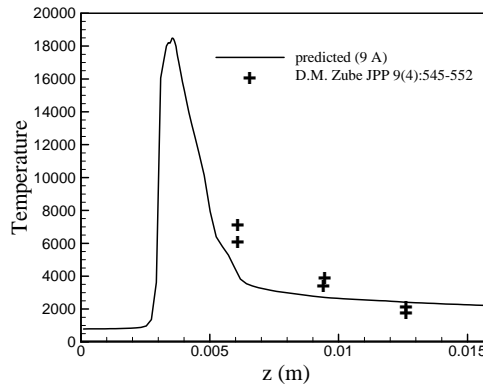
Fig. 5 Comparisons of computed axial velocity (a) and temperature (b) profiles at the exit plane for different viscosity values. CASE 1: with simulated hydrazine as the propellant, inlet stagnant pressure 3.3×10^5 Pa and arc current 9 A; and CASE 2: with pure hydrogen as propellant, inlet stagnant pressure 2.5×10^5 Pa and arc current 10 A. 1.0μ means actual viscosity is used; 0.1μ means 0.1 times actual viscosity is used.

(a) Comparison of temperature along the arcjet nozzle axis with simulated hydrazine as propellant.
Modeling parameters: mass flow rate is 44.8 mg/s and arc current is 9A.
Experimental parameters: mass flow rate is 47.6 mg/s and arc current is 9A.
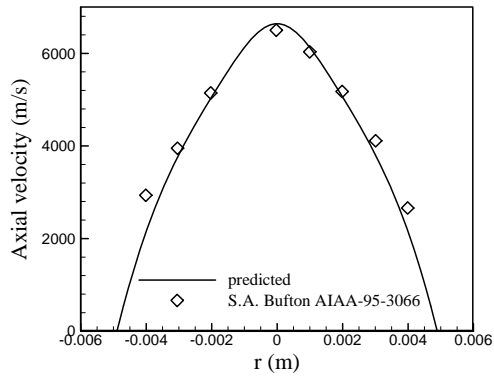
(b) Comparison of temperature along the arcjet nozzle axis with simulated hydrazine as propellant.
Modeling parameters: mass flow rate is 50.1 mg/s and arc current is 10A.
Experimental parameters: mass flow rate is 50 mg/s and arc current is 10A.

Fig. 6 Comparisons of computed results and experimental data concerning the axial variation of gas temperature along the nozzle axis (a) and the radial profile of axial-velocity at the exit plane (b) for the simulated hydrazine arcjet. The arc current is 9 A for (a) and 10 A for (b).